Emiss. Control Sci. Technol. (2016) 2:115–123
DOI 10.1007/s40825-016-0042-2

Formation of Urea-Based Deposits in an Exhaust System: Numerical Predictions and Experimental Observations on a Hot Gas Test Bench

Wolfgang Brack[1,3] · Barbara Heine[1] · Felix Birkhold[1] · Matthias Kruse[1] · Olaf Deutschmann[2]

Received: 10 September 2015 / Revised: 28 November 2015 / Accepted: 11 May 2016 / Published online: 16 June 2016

Abstract Using a generic configuration of an exhaust system, the formation of deposits due to urea-derived by-products is examined. For this purpose, the temporal profile of the formation of deposits is visually observed and the resulting deposit composition is analyzed. Based on the experimental results, the most important deposit regime can be identified depending on the measured wall temperatures and is compared with the prediction of a suitable reaction mechanism.

Keywords Urea · By-product · Deposit · SCR · AdBlue · Dosing

1 Introduction

Stricter emission limits for lean burning engines require individually adapted concepts of measures inside the engine as well as exhaust gas after-treatment systems to reduce nitrogen oxide (NOx) and soot emissions. The selective catalytic reduction (SCR) is a promising and widely used solution to achieve the required reduction in NOx emissions [11, 13]. To supply the reducing agent ammonia, an aqueous 32.5 %-wt urea solution (AdBlue) is used for reasons of toxicity and safety [2].

The processing of the aqueous urea solution to the reducing medium ammonia must take place before entering the catalyzer inlet. After the evaporation of the water fraction in the AdBlue droplets, the thermal decomposition of the urea takes place in the droplets (urea thermolysis according to Eq. 1, with states of aggregation: (m): molten, (g): gaseous and (l): liquid/dissolved), and the isocyanic acid formed evaporates quickly.

$$\underset{\text{urea}}{CO(NH_2)_{2\,(m)}} \longrightarrow \underset{\text{isocyanic acid}}{HNCO_{\,(l)}} + \underset{\text{ammonia}}{NH3_{\,(g)}} \quad (1)$$

Usually, the evaporation of isocyanic acid is included in the formulation of the thermolysis reaction [3, 4]. However, for a detailed investigation of the chemical reactions in a liquid film, it is necessary to treat the chemical reactions as well as the evaporation processes separately. In the gaseous phase as well as on the catalyst surface, the isocyanic acid can hydrolyze to ammonia and carbon dioxide (Eq. 2).

$$\underset{\text{isocyanic acid}}{HNCO_{\,(g)}} + \underset{\text{water}}{H_2O_{\,(g)}} \longrightarrow \underset{\text{ammonia}}{NH_{3\,(g)}} + \underset{\text{carbon dioxide}}{CO_{2\,(g)}} \quad (2)$$

For the best possible NOx conversion, the resulting ammonia must be distributed homogeneously over the catalyzer cross-section since material transport between separate monolith channels is not possible in the catalyzer. Furthermore, it must be guaranteed that the urea injected reacts to ammonia instead of forming a wall film or any solid by-products. Formation of wall film occurs as a result of the spray-wall interaction when the wall temperature is below the Leidenfrost temperature. In the liquid film, chemical reactions can take place since the isocyanic acid is very

✉ Wolfgang Brack
wolfgang.brack@bmw.de

[1] Robert Bosch GmbH, Robert-Bosch-Platz 1, 70049 Stuttgart, Germany

[2] Institute for Chemical Technology and Polymer Chemistry, Karlsruhe Institute of Technology (KIT), Kaiserstr. 12, 76128 Karlsruhe, Germany

[3] Present address: BMW Group, 80788 Munich, Germany

reactive [14]. This can lead to the formation of solid urea reaction products for suitable temperatures and a sufficient residence time within the liquid film. This urea-derived by-product formation has to be avoided for robust system behavior, including an error-free operation of an AdBlue dosing module. The formation of deposits can lead to the failure of the dosing strategy. Consequently, the SCR system cannot reach the maximum possible NOx conversion, and the decomposition of the formed urea-derived by-products can result in an ammonia slip. Moreover, the deposits formed may clog the exhaust pipe or, at least, increase the pressure drop.

Figure 1 shows the formation of deposits in the exhaust pipe. Here, two of the three spray plumes are directed toward the pipe wall, leading to local cooling of the wall in the region of the spray impact area. These can be clearly recognized in the thermal image measurement, showing the bottom side of the exhaust pipe. For wall temperatures below the Leidenfrost temperature, a liquid wall film is formed. This film evaporates and, because of the resulting enthalpy of evaporation, causes increased local cooling of the wall. In addition, the liquid film flows downstream and passes different regions of wall temperatures. Depending on the wall temperature and the residence time, the urea in the wall film can react there to urea-derived by-products. This process can be seen as white deposits downstream in the middle of the pipe in Fig. 1. The chemical composition of the deposits can be calculated on the basis of a reaction mechanism developed by Brack et al. [5], depending on the film temperature, the residence time and the thickness of the wall film. Based on the results of simulations, the critical wall temperatures for the formation of deposits are found. Analogously, the formation of deposits in an exhaust system is studied on a hot gas test bench and is compared to the simulation data. Consequently, the main regimes of urea-derived by-product formation are identified.

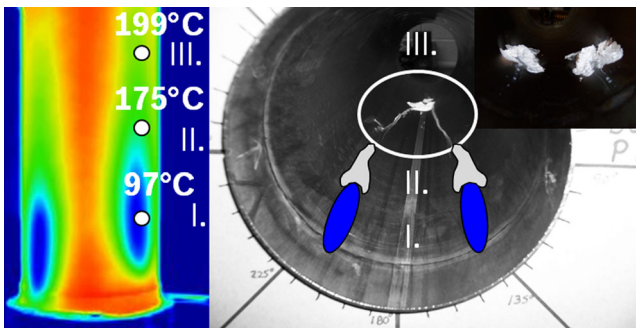

Fig. 1 Mechanism of urea-derived by-products formation in an exhaust system: spray-wall interaction results in local cooling of the wall as well as in formation of a liquid film (I.). The liquid film flows downstream and passes different regions of wall temperatures (II.). Formation of urea-derived by-products in hotter areas (III.)

2 Methods

2.1 Simulation of Chemical Reactions

In addition to the desired reaction path, isocyanic acid dissolved in the liquid film can react with urea to form solid biuret. Solid biuret melts and decomposes above 193 °C [14], mostly to cyanuric acid, which decomposes to gaseous isocyanic acid at temperatures above 250 °C. Furthermore, both small amounts of ammelide, which can react to form ammeline and melamine, and small amounts of triuret are formed. Triuret decomposes to cyanuric acid above approximately 220 °C. The most important reaction paths are described in accordance with the reaction mechanism of Brack et al. [5], as summarized in Table 1.

The reaction mechanism is based on a continuous stirred-tank reactor (CSTR) approach, with the assumptions of perfect mixing and a homogeneous temperature distribution. Since the rapid evacuation of the resulting gaseous decomposition products is guaranteed and their mass contribution to the exhaust gas mass flow is negligible, gas phase reactions are not considered here.

Consequently, the rate of conversion of the species i can be calculated in terms of the change of the molar amount per time unit $\frac{dn_i}{dt}$, for each species i, where the rate of conversion of i is linked by the corresponding stoichiometric factor $\nu_{i,r}$ to the change of the reaction r over the time $\frac{dn_r}{dt}$.

$$\frac{dn_i}{dt} = \sum_{r=I}^{XV} \nu_{i,r} \cdot \frac{dn_r}{dt} + j_i \tag{3}$$

For reaction equations II up to XIV (Table 1), the reaction rate $\frac{dn_r}{dt}$ can be calculated using Eq. 4.

$$\frac{dn_r}{dt} = A_0 \cdot \mathrm{e}^{\frac{-E_A}{RT}} \cdot V_\mathrm{R} \cdot \prod^{j} c_j^{\gamma_j} \ , \quad r \in \{II, III, \ldots, XIV\} \tag{4}$$

Here, V_R is the volume of the reactor and c_j is the concentration of the educt species j, with a reaction order of γ_j, A_0 is the pre-exponential factor of the reaction, E_A is the activation energy of the reaction, and R is the universal gas constant. Since the decomposition of cyanuric acid does not depend on the concentration of cyanuric acid, the reaction equation I (Table 1) is normalized to the ratio of the surface area A_R to the reference surface area A_ref of 14.52 mm^2. This is meant to guarantee a decomposition rate that is independent of the surface discretization.

$$\frac{dn_r}{dt} = A_0 \cdot \mathrm{e}^{\frac{-E_A}{RT}} \cdot \frac{A_\mathrm{R}}{A_\mathrm{ref}} \ , \quad A_\mathrm{ref} = 14.52\ mm^2, \quad r \in \{I\} \tag{5}$$

The evaporation of dissolved isocyanic acid is modeled to capture geometric effects on the decomposition behavior. To

Table 1 Kinetic reaction scheme of urea decomposition taken from Brack et al. [5]

	Reaction	Pre-exponential factor A_0	Activation energy E_A
I	CYA $_{(s)}$ ⟶ 3 HNCO $_{(g)}$	1.001×10^{03} mol/s	118.42 kJ/mol
II	biuret $_{(m)}$ ⟶ urea $_{(m)}$ + HNCO $_{(l)}$	1.107×10^{20}/s	208.23 kJ/mol
III	urea $_{(m)}$ + HNCO $_{(l)}$ ⟶ biuret $_{(m)}$	3.517×10^{11} ml/(mol s)	75.45 kJ/mol
IV	urea $_{(m)}$ ⟶ HNCO $_{(l)}$ + NH_3 $_{(g)}$	2.000×10^{04} mol $^{0.7}$/(ml $^{0.7}$s)	74.00 kJ/mol
V	2 biuret $_{(m)}$ ⟶ ammelide $_{(s)}$ + HNCO $_{(l)}$ + NH_3 $_{(g)}$ + H_2O $_{(g)}$	3.637×10^{26} ml/(mol s)	257.76 kJ/mol
VI	biuret $_{(m)}$ + HNCO $_{(l)}$ ⟶ CYA $_{(s)}$ + NH_3 $_{(g)}$	9.397×10^{20} ml/(mol s)	158.68 kJ/mol
VII	biuret $_{(m)}$ + HNCO $_{(l)}$ ⟶ triuret $_{(s)}$	1.091×10^{15} ml/(mol s)	116.97 kJ/mol
VIII	triuret $_{(s)}$ ⟶ CYA $_{(s)}$ + NH_3 $_{(g)}$	1.238×10^{18}/s	194.94 kJ/mol
IX	urea $_{(m)}$ + 2 HNCO $_{(l)}$ ⟶ ammelide $_{(s)}$ + H_2O $_{(g)}$	1.274×10^{20}ml^2/(mol^2 s)	110.40 kJ/mol
X	biuret $_{(m)}$ ⟶ biuret $_{(matrix)}$	8.193×10^{26}/s	271.50 kJ/mol
XI	biuret $_{(matrix)}$ ⟶ biuret $_{(m)}$	3.162×10^{09}/s	122.00 kJ/mol
XII	biuret $_{(matrix)}$ ⟶ 2 HNCO $_{(g)}$ + NH_3 $_{(g)}$	5.626×10^{24}/s	266.38 kJ/mol
XIII	urea $_{(s)}$ ⟶ urea $_{(m)}$	$1.000 \times 10^{15} \cdot T^{1.5}$/s	160.00 kJ/mol
XIV	ammelide $_{(s)}$ ⟶ ammelide $_{(g)}$	1.000×10^{14}/s	201.67 kJ/mol
XV	HNCO $_{(l)}$ ⟶ HNCO $_{(g)}$	Equation 6, $\alpha_c = 0.001$	

States of aggregation: (s): solid, (m): molten, (g): gaseous, (l): liquid/dissolved, (matrix): solid matrix. No gas phase reactions are considered. Ammelide: $C_3N_3(OH)_2NH_2$, ammonia: NH_3, biuret: H_2N-CO-NH-CO-NH_2, cyanuric acid (CYA): $C_3N_3(OH)_3$, isocyanic acid: HNCO, triuret: H_2N-CO-NH-CO-NH-CO-NH_2, urea: $CO(NH_2)_2$, water: H_2O, α_c: accommodation coefficient

serve this purpose, the CSTR is extended by an ansatz for the absorption and desorption of non-reacting gases across a planar surface [10], represented by source term j_i for the evaporation of the dissolved species i. This is necessary because the surface-to-volume ratio is identified as a crucial parameter regarding the risk of cyanuric acid formation [5, 9]. Since a smaller available surface area causes lower evaporation rates of isocyanic acid, the dissolved isocyanic acid has more time to react to cyanuric acid. The source term j_i for the evaporation of the dissolved species i can be calculated with the mean thermal velocity $\overline{v}$ of the gas molecules, the accommodation coefficient α_c and the species concentrations $c^{S}_{i,1}$, which are linked together by the Henry Law's constant h.

$$j_i = \frac{1}{4} \cdot \alpha_c \cdot \overline{v} \cdot \frac{c^{S}_{i,1}}{h} \cdot A_R \tag{6}$$

with:

$$\overline{v} = \sqrt{\frac{8 \cdot R \cdot T}{\pi \cdot M}} \tag{7}$$

$$h = \frac{c_{liq}{}^{eq}}{c_{gas}{}^{eq}} = \frac{\rho_{liq}}{p_{vap} \cdot \frac{M}{R \cdot T}} \tag{8}$$

Here, M is the molar mass of the dissolved species, ρ is the density, and A_R is the surface area. p_{vap} represents the vapor pressure of the dissolved species, which can be described for isocyanic acid by Eq. 9 [12].

$$p_{vap,\ HNCO} = 10^{4.69 - \frac{1252.195}{\frac{T}{K} - 29.167}} \quad \text{bar} \tag{9}$$

The resulting coupled governing equations are solved, using the semi-implicit solver LIMEX [8]. For this purpose, a stand-alone Fortran code, based on DETCHEM^{EVAPORATOR} [6], is used.

2.2 Simulation of Spray-Wall Impingement

An existing wall film is a prerequisite for the formation of solid by-products. Such wall wetting occurs as a result of the spray-wall interaction when the wall temperature is below the Leidenfrost temperature. Since the local cooling of the wall in the region of the spray impact surfaces corresponds to the spray impact density, the place, where the cooling of the wall is maximal, can be estimated by evaluating the spray surface load (SSL). This value is the impinged mass flow rate of AdBlue per square centimeter.

For this purpose, the commercial CFD-code AVL FIRE v2013.2 [1] is used. Here, the spray is modeled by a Lagrangian ansatz based on a statistical method referred to

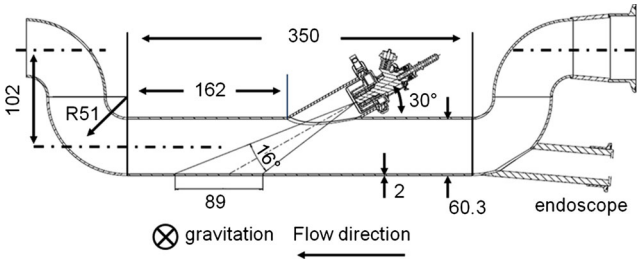

Fig. 2 Geometry: U-shaped pipe. All dimensions in (mm)

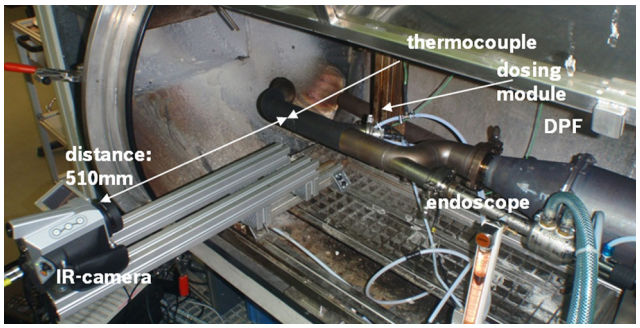

Fig. 3 U-shaped exhaust system on a hot gas test bench

as the discrete droplet method (DDM) [7]. The sub-models for evaporation as well as for spray-wall interaction are valid for the use of AdBlue [3, 4].

2.3 Experiment

The experimental study is carried out on a hot gas test bench with an U-shaped exhaust system, the inner pipe diameter of which, similar to an inner pipe diameter typically used in the automobile sector, amounts to 56.3 mm. The wall thickness of the pipes used is 2 mm and they are made of stainless steel (X5CrNi18-10). Prior to and after the dosing location, two oppositely oriented 90° direction changes are mounted. Figure 2 shows the geometry that is used, and Fig. 3 shows the setup on the hot gas test bench. For a more detailed characterization of the formation of deposits, an endoscope is introduced through an optical access point. A high-temperature endoscope made by Schölly (SO HT-0017) with a camera by IDS (UI-2240RE-C-HQ) is used. Since a gas burner is used for generating hot gas, a diesel particulate filter (DPF) is connected upstream to the U-pipe in order to ensure a homogeneous velocity distribution as well as the functional capability of the endoscope during the operation of the test bench. Furthermore, the wall temperature is measured with a thermocouple and a thermal imaging camera made by Infratec (VarioCam). In order to achieve an emissivity that is as defined and uniform as possible, the measuring area is painted black. For dosing, two different three-hole injectors with a spray angle α of 10° and 16° are used. In each case, the injection pressure is 5 bar and the theoretical impact area for the spray of both injectors is

Table 2 Spray data of used injectors

Injector	α (°)	SMD (μm)	Dv90 (μm)	Q_{stat} ($^{mg}/_{s}$)	Velocity ($^{m}/_{s}$)
3-hole (Bosch)	10	173	346	860	24
3-hole (Bosch)	16	91	238	879	24

Table 3 Operation points

OP –	Exhaust gas temperature (°C)	Exhaust gas massflow ($^{kg}/_{h}$)	α (°)
1	215	100	16
2	300	200	10
3	440	300	16

completely in the direct middle section of the exhaust system. The dosage is pulsed, i.e., the quantity of the dosage is controlled by the duty cycle, which indicates the percentage of time of the open injector. Consequently, the dosing rate $\dot{m}_{dos}$ can be calculated by Eq. 10, depending on the maximum static flow rate Q_{stat} of the injectors used.

$$\dot{m}_{dos} = DC \cdot Q_{stat} \tag{10}$$

For experimental evaluations, a constant injection frequency f of 3.3 Hz is used. The spray data of both injectors was determined experimentally by optical measuring techniques and are summarized in Table 2. The size distribution of spray droplets, including the Sauter mean diameter (SMD) as well as the Dv90, is measured by Malvern method, and the initial velocity of the droplets is given by phase Doppler anemometry. The diameter of the circle perpendicular to the nozzle axis that passes through the center of the nozzle holes [1] is 1.9 mm and the outer diameter of each hole is 0.12 mm. The circular hole distribution of the three holes is homogeneous (120°) with a hole position toward the connector of 0°. The cone angle of one spray plume β is in the case of the 10°-injector 4.8° and in the case of the 16°-injector 6.6°.

The operation points used for this investigation (Fig. 4) are based on critical operation points regarding risk of urea-derived by-products, identified in several passenger car applications. The evaluation of the critical dosing amount, i.e., the dosing amount formation of deposits observed first, can be characterized by three characteristic operation points

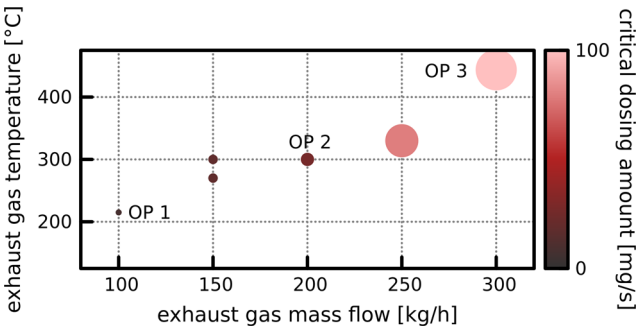

Fig. 4 Operation points including their critical dosing amount. OP 1: 8 $^{mg}/_{s}$, OP 2: 26 $^{mg}/_{s}$ and for OP 3 no deposits are visible up to 220 $^{mg}/_{s}$

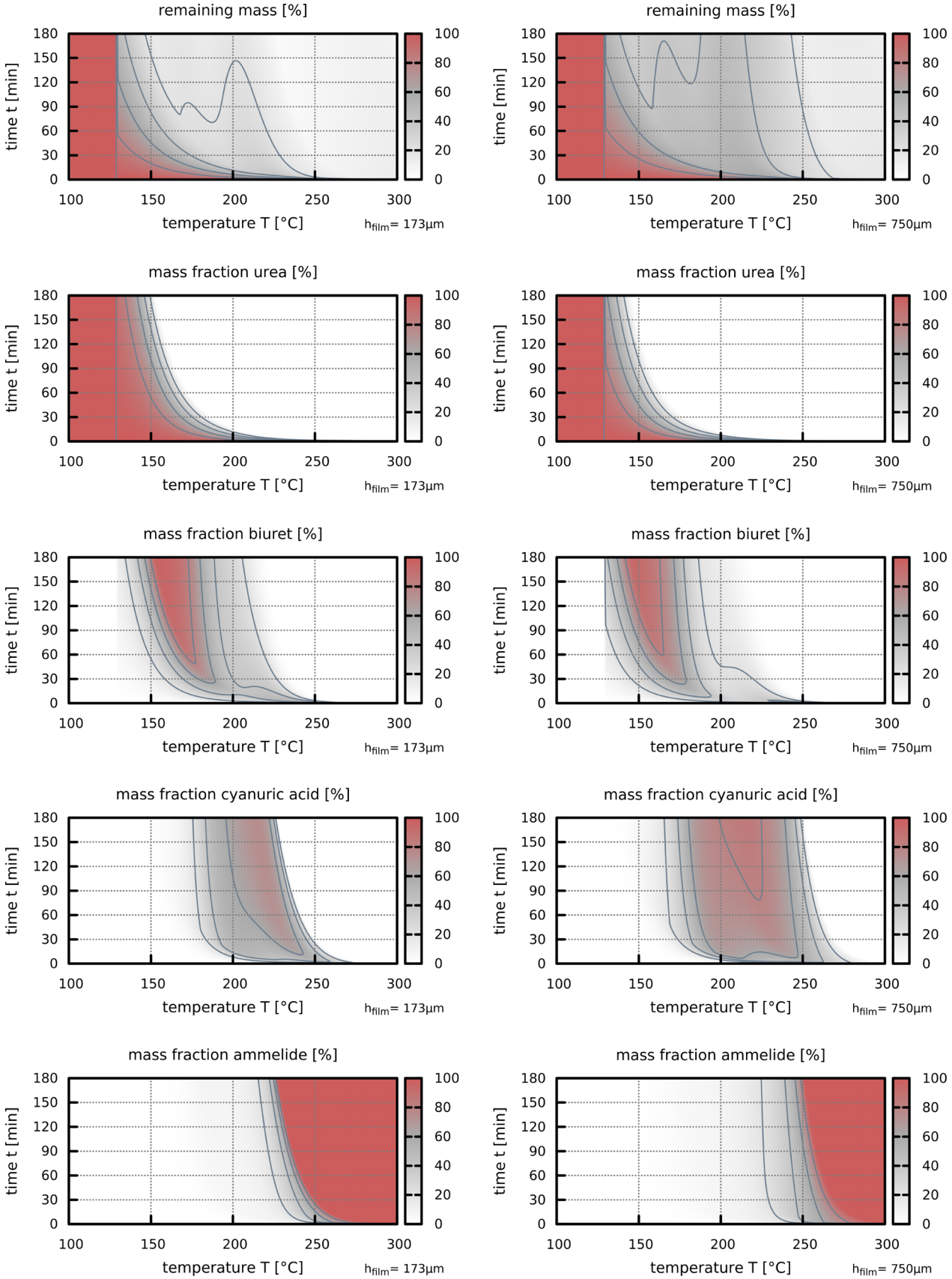

Fig. 5 Calculated remaining mass and mass fraction of species for a film thickness of $h_{\mathrm{film}} = 173\ \mu$m (*left*) and 750 μm (*right*)

summarized in Table 3. For the determination of the critical dosage, the duty cycle is increased in discrete steps until deposits can be observed in the exhaust pipe.

3 Results and Discussion

In general, the formation of solid urea-derived by-products starts upon wall wetting. The expected amount of deposits and the chemical composition of the deposits can be calculated as a function of the film temperature, the residence time, and the film thickness. Since the heat conduction between the pipe wall and the film is several times greater than the convective heat flow between the film and the gaseous phase, the film temperature for the stationary state can be approximated by measuring the wall temperatures. For the chemical reactions, the temperatures in the peripheral areas of the film are decisive because the formation of deposits is initially in these areas. Since the evaporation of the film barely influences the wall temperatures in these peripheral areas of the wall film, temperatures prevailing there are similar to those temperatures occurring without the dosage. The thickness of the wall film h_{film} is assumed to be 173 μm for a moving liquid film, equal to the Sauter mean diameter of the 10°-injector, and 750 μm for a stagnant film. However, the findings for the film thickness of 750 μm are also valid for a higher film thickness. A stagnant film occurs if the liquid wall film is dammed at the deposits formed. A measurement of the film thickness is not possible on the test bench used.

Figure 5 shows the calculated remaining mass as well as the calculated mass fractions of the species. The influence of the thickness of the film can be confirmed by the calculation results, which show a clear effect on the part of the amount of the film. The results for a thickness of the film of 173 μm are shown on the left in contrast to the results for a higher thickness of the film on the right. The thicker the film, the greater the amount of cyanuric acid is. The unfavorable surface-to-volume ratio is responsible for this behavior [5] because a thicker film causes a lower available surface area for the evaporation of isocyanic acid if the volume is constant. Therefore, there is more dissolved isocyanic acid in the film that can react with cyanuric acid.

From the calculated mass fractions, the distribution of species massfraction depends on the temperature. With increasing temperature, urea is observed at first, followed by biuret, cyanuric acid, and ammelide. However, with increasing temperatures, the total mass of the deposits decreases (Fig. 5, top). Consequently, three deposit regimes can be distinguished. In the low-temperature range, of up to approximately 150 °C, no formation of urea-derived by-products takes place. Here, only crystalline urea exists as a solid. A temperature range from 150 °C up to approximately 250 °C is very prone to the formation of deposits since large quantities of biuret and cyanuric acid are formed. At temperatures above 250 °C, heat-resistant ammelide exits almost exclusively. However, the amount of ammelide is rather low. Such an operating range is usually not critical, except with a very long operating time. In general, the formation of deposits depends on the wall temperatures and on the residence time of the film.

In the experimental test setup, the three spray beams of the injection valve are aligned to the opposite wall. Depending on the selected flow rate and the gas temperature, the drift of the spray is more or less. This results in a different impact density of the spray on the wall, whereas the impact density is directly correlated with the wall cooling. The higher the maximum impact density, the higher the local cooling of the wall through the spray.

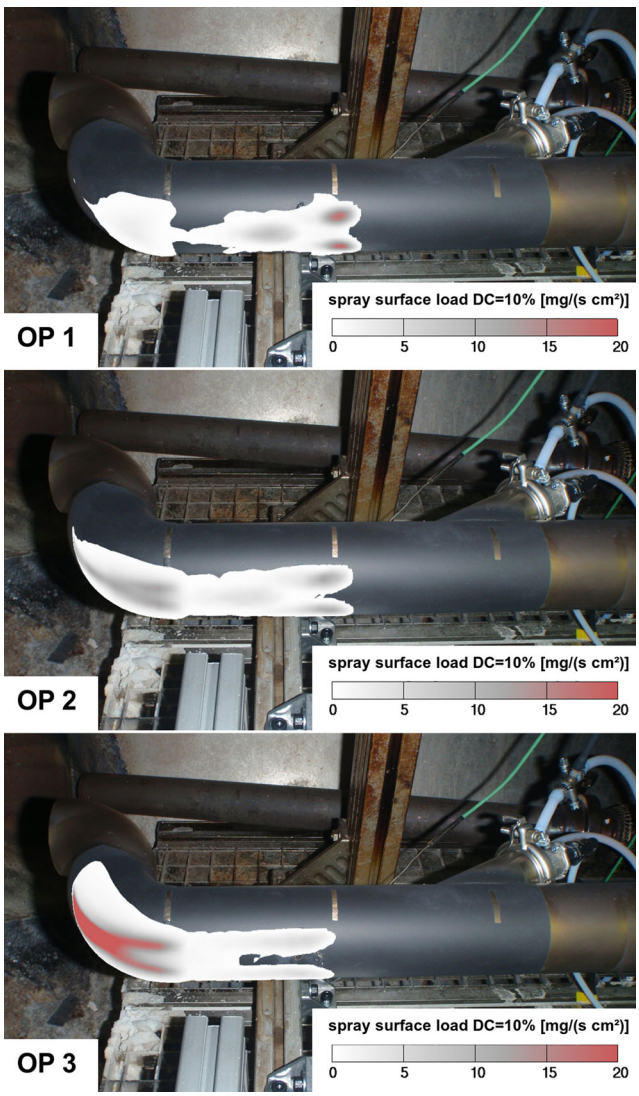

Fig. 6 Calculated spray surface load. From *top* to *bottom*: OP 1, OP 2, OP 3

Figure 6 shows the computed spray impact densities, characterized by the spray surface load value for the three operating points. The defined values apply to the 10°-injection valve with a duty cycle DC of 10 %, and represent all drop-wall interactions that take place, including the multiple contacts of individual drops that may occur if the drops splash or rebound on a hot pipe wall. The stronger drift of the spray with an increasing exhaust velocity can be seen. From the results, the initial deposit location can be estimated. At hot wall temperatures, in combination with high exhaust gas mass flows, multiple contacts of spray droplets tend to occur and the spray impact density is at its maximum in the area of the pipe bend. Consequently, the local cooling in the pipe bend area is the strongest and the wall is most likely to become wet there. In contrast, at cold wall temperatures, the first contact of the drops is crucial. This is at a maximum in the area of the straight pipe piece opposite the injection flange. Correspondingly, the commencement of deposits against the injection flange is to be expected at such operating points.

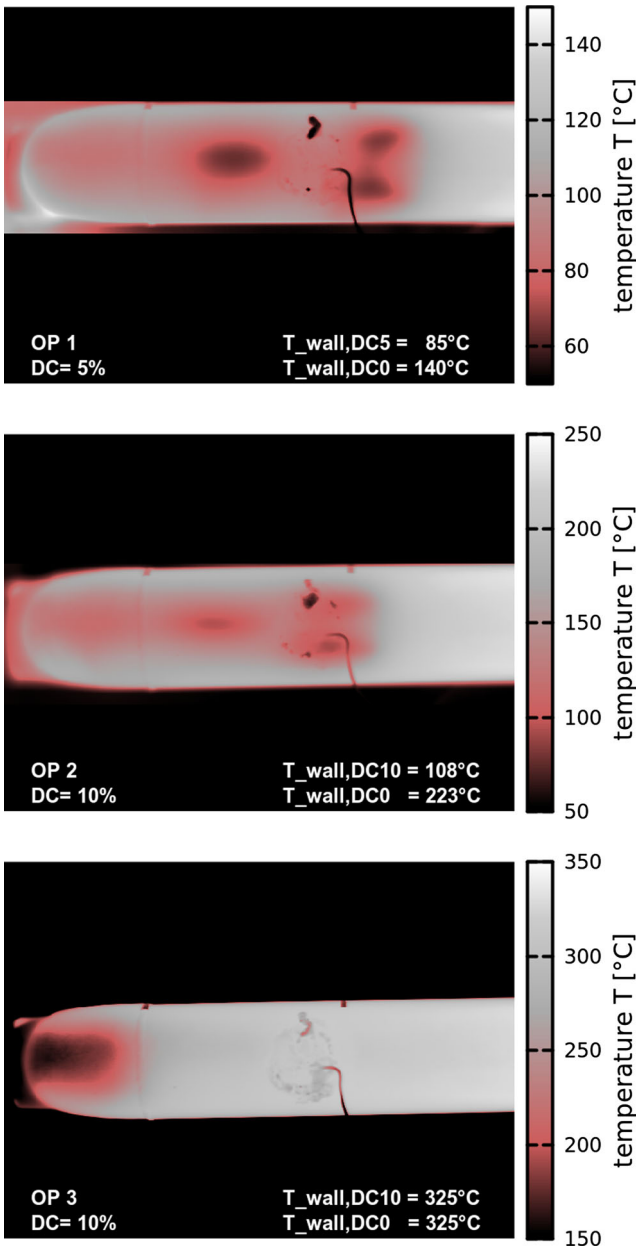

Fig. 7 Measured temperature of the outer wall depending on infrared measurements. From *top* to *bottom*: OP 1, OP 2, OP 3. The flow direction is from right toward left. T_{wall}: temperature measured by the thermocouple

The corresponding measurements of the wall temperature by means of an infrared camera are shown in Fig. 7. However, it must be noted that both the connection of the attached thermocouple and the solder joints in the thermal images are clearly recognizable as imperfections, and no evaluation can take place in such areas. The evaluated wall temperatures are based on an estimated emissivity ϵ of 0.9. In addition, the comparative value of the temperature measurement value is performed by the thermocouple. The infrared images clearly show the cooling locations on the basis of the spray-wall interaction of the spray beams that arises and are in accordance with the predicted spray impact densities in Fig. 6. In the case of OP 1, the wall temperatures are evaluated by a duty cycle of 5 % because the pipe is completely wetted at a duty cycle of 10 %.

As the endoscopic image shows in Fig. 8, at a cold operating point (OP 1), only liquid wetting of the pipe wall is observed. The liquid film is discharged at the end of the pipe and crystallizes at the bottom of the test bench cell. At a high amount of dosing, solid deposits can be observed in the area of the dosing flange because even a low spray-wall interaction or a small liquid leakage of the dosing module at this operating point causes a wetting of the wall. The analysis of the deposits is in accordance with the numerical predictions since urea and small amounts of biuret are mainly present at the existing low wall temperatures ($T_{\text{wall}} < 140$ °C). The sampling is carried out at the end of

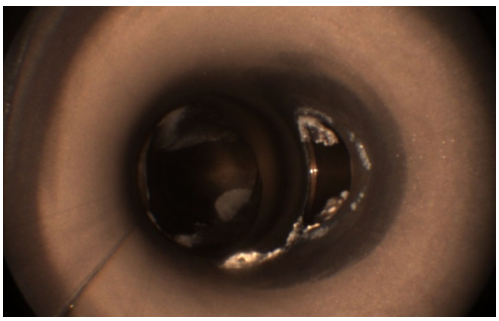

Fig. 8 Formation of urea-derived by-products: OP 1, duty cycle $DC = 20$ %

Table 4 Species mass fractions of existing deposits based on HPLC analysis

OP -	Wall temperature ($DC = 0$ %) (°C)	Urea (w. %)	Biuret (w. %)	Cyanuric acid (w. %)	Triuret (w. %)	Ammelide (w. %)	Ammeline (w. %)	Melamine (w. %)	Total (w. %)
1	140	94.3	7.3	0.0	0.2	0.0	0.0	0.0	101.8
2	223	0.8	0.5	80.3	0.0	18.2	3.0	0.1	102.9
3	325	No urea-derived by-products							

the test, and represents a good approximation of a mixture of all existing deposits. The data of high-performance liquid chromatography (HPLC) is summarized in Table 4. Since no damming of the wall film can be observed where the deposits are formed, the calculated species mass fractions for a low film thickness of 173 μm (Fig. 5, left series of graphs) are relevant for comparison with the simulation. For a temperature range of 130 to 140 °C, the simulation predicts a urea mass fraction of the deposits between 80 and 100 %. In general, the mass fraction of urea increases as the film temperatures and thickness decrease. Despite the negligible formation of solid urea-derived by-products, such an operating point in a real-world application should be avoided since the liquid wall film may flow directly into the catalyzer leading to a functional impairment of the catalyzer.

In the case of the second operating point (OP 2), significant quantities of solid deposits arise. At a high dosage, these deposits could block the pipe completely. Figure 9 shows the urea-derived by-products existing after 400 min for OP 2. The duty cycle DC is increased in steps of 0.5 % every 10 min. The formation of deposits begins in the pipe bend area and, with an increasing quantity of the dosage, expands upstream in the direction of the impact point of the spray. The corresponding thermal images presented in Fig. 7 initially show a significant cooling in the area of the pipe bend as a consequence of an incipient formation of wall film. This location corresponds to the location of the maximum spray impact density, as shown in Fig. 6. The prevailing wall temperatures in the peripheral areas of the wall film favor the formation of solid urea-derived by-products. The existing wall film may accumulate on the deposits that have formed. The experimental observations clearly show a more rapid growth rate of the deposits after an initial period of solid formation. Consequently, an accumulation of the wall film must be avoided. In this case, the calculation results for a high thickness of the film are relevant. As in the numerical predictions (Fig. 5), an analysis of the deposits (Table 4) reveals cyanuric acid as the main component of the deposits in a wall temperature range of 200 to 225 °C. Ammelide is detected in significant quantities as well. This formation of ammelide was also computed, but to a lower extent.

At high exhaust gas temperatures and mass flows, no formation of deposits can be observed (Fig. 10) because the temperatures in the peripheral areas of the film are too high, such that solid deposits can be formed in large quantities there. In contrast to the previous operating points, the impact points of the spray beams are, based on the higher flow rate and the associated stronger drift of the spray beams, completely in the area of the pipe bend, as the evaluation of spray impact density in Fig. 6 shows. Therefore, only one cooling spot in the area of the pipe bend is visible on the corresponding infrared image (Fig. 7). The negligible amount of deposits formed agrees with the model predictions (Fig. 5). For wall temperatures above 300 °C, only a very low total quantity of ammelide is formed according to the numerical simulation.

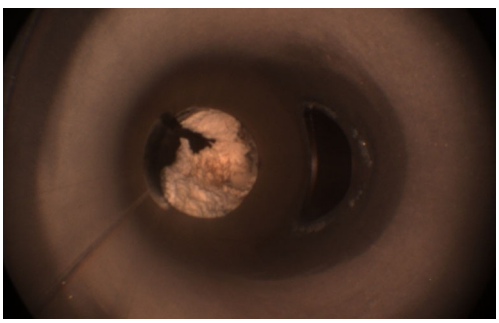

Fig. 9 Formation of urea-derived by-products: OP 2, duty cycle $DC = 20$ %

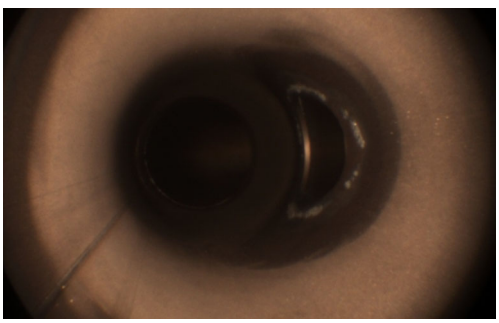

Fig. 10 Formation of urea-derived by-products: OP 3, duty cycle $DC = 20$ %

4 Conclusions

The reaction mechanism for the thermal decomposition of urea, developed in our earlier work under laboratory conditions [5], could be successfully transferred to an exhaust system. In line with the experimental results, three regimes for the formation of deposits can be identified:

- Cold operation conditions ($T_{wall} < 150\,°C$), represented by OP 1; mainly crystalline urea exists as a solid.
- Critical operation conditions ($150\,°C < T_{wall} < 250\,°C$), represented by OP 2; significant quantities of biuret, cyanuric acid and ammelide are formed.
- Hot operating conditions ($T_{wall} > 250\,°C$), represented by OP 3; only low quantities of ammelide are formed.

The local maximum cooling due to the spray-wall interaction corresponds well with the evaluation of the maximum spray surface load in the simulation. This provides an opportunity to adapt the characteristics of the spray individually for different exhaust systems. However, it is not possible to draw conclusions based on the evaluation of the spray surface load if solid by-products are formed. The spray surface load value is only an indicator of wall wetting. A reliable quantitative prediction of the deposit risk through a numerical simulation still remains a topic of research even though this study has revealed the potential of the currently available chemical models for qualitative predictions. It is necessary to calculate the prevailing wall temperatures as well as the thickness of wall film during the formation of urea-derived by-products. Consequently, detailed models for mass and heat transport as well as for the liquid film, including chemical reactions in the liquid, have to be coupled in numerical simulation.

Acknowledgments We thank the Steinbeis GmbH für Technologietransfer (STZ 240 Reaktive Strömungen) for a fruitful collaboration concerning the use of the software DETCHEM^{TM}. O.D. acknowledges support by the Deutsche Forschungsgemeinschaft through SFB/Transregio 150 project B05.

References

1. AVL List Gmbh: AVL FIRE user manual v2013, Graz (2013)
2. Ball, J.: A toxicological evaluation of potential thermal degradation products of urea, SAE technical paper, 2001-01-3621 (2001)
3. Birkhold, F., Meingast, U., Wassermann, P., Deutschmann, O.: Analysis of the Injection of Urea-water-solution for automotive SCR deNOx-systems: Modeling of Two-phase Flow and Spray/Wall-Interaction, SAE Technical Paper 2006-01-0643 (2006)
4. Birkhold, F., Meingast, U., Wassermann, P., Deutschmann, O.: Modeling and simulation of the injection of urea-water-solution for automotive SCR deNOx-systems. Appl. Catal. Environ. **70**, 119–127 (2007)
5. Brack, W., Heine, B., Birkhold, F., Kruse, M., Schoch, G., Tischer, S., Deutschmann, O.: Kinetic modeling of urea decomposition based on systematic thermogravimetric analyses of urea and its most important by-products. Chem. Eng. Sci. **106**, 1–8 (2014)
6. Deutschmann, O., Tischer, S., Correa, C., Chatterjee, D., Kleditzsch, S., Janardhanan, V.M., Mladenov, N., Minh, H.D., Karadeniz, H., Hettel, M.: DETCHEM Software package, 2.5 ed, www.detchem.de, Karlsruhe (2014)
7. Dukowicz, J.K.: A particle-fluid numerical model for liquid sprays. J. Comput. Phys. **35**, 229–253 (1980)
8. Ehrig, R., Nowak, U., Oeverdieck, L., Deuflhard, P.: Advanced extrapolation methods for large scale differential algebraic problems. High Performance Scientific and Engineering Computing **8**, 233–244 (1999)
9. Eichelbaum, M., Farrauto, R.J., Castaldi, M.: The impact of urea on the performance of metal exchanged zeolites for the selective catalytic reduction of NOx: Part I. Pyrolysis and hydrolysis of urea over zeolite catalysts. Appl. Catal. Environ. **97**, 90–97 (2010)
10. Huthwelker, T., Peter, T.: Analytical description of gas transport across an interface with coupled diffusion in two phases. J Chem Phys **105**, 1661–1667 (1996)
11. Koebel, M., Elsener, M., Kleemann, M.: Urea-SCR: a promising technique to reduce NOx emissions from automotive diesel engines. Catal. Today **59**, 335–345 (2000)
12. Linhard, M.: Der Dampfdruck flüssiger Cyansäure. Zeitschrift für anorganische und allgemeine Chemie **236**, 200–208 (1938)
13. Moser, F.X., Sams, T., Cartellieri, W.: Impact of future exhaust gas emission legislation on the heavy duty truck engine, SAE technical paper 2001-01-0186 (2001)
14. Schaber, P.M., Colson, J., Higgins, S., Thielen, D., Anspach, B., Brauer, J.: Thermal decomposition (pyrolysis) of urea in an open reaction vessel. Thermochim. Acta **424**, 131–142 (2004)